


 Cite this: *RSC Adv.*, 2023, **13**, 8873

# Interface engineering of $\text{CeO}_2$ nanoparticle/ $\text{Bi}_2\text{WO}_6$ nanosheet nanohybrids with oxygen vacancies for oxygen evolution reactions under alkaline conditions†

 Dukhyun Nam,<sup>a</sup> Geunhyeong Lee<sup>a</sup> and Jooheon Kim<sup>ID, \*abc</sup>

Because of the interactive combination synergy effect, hetero interface engineering is used way for advancing electrocatalytic activity and durability. In this study, we demonstrate that a  $\text{CeO}_2/\text{Bi}_2\text{WO}_6$  heterostructure is synthesized by a hydrothermal method. Electrochemical measurement results indicate that  $\text{CeO}_2/\text{Bi}_2\text{WO}_6$  displays not only more OER catalytic active sites with an overpotential of 390 mV and a Tafel slope of 117 mV dec<sup>-1</sup> but also durability for 10 h (97.57%). Such outstanding characteristics are primarily attributed to (1) the considerable activities by  $\text{CeO}_2$  nanoparticles uniformly distributed on  $\text{Bi}_2\text{WO}_6$  nanosheets and (2) the plentiful Bi–O–Ce and W–O–Ce species playing the role of strong couples between  $\text{CeO}_2$  nanoparticles and  $\text{Bi}_2\text{WO}_6$  nanosheets and oxygen vacancy existence in  $\text{CeO}_2$  nanoparticles, which can improve the electrochemical active surface area (ECSA) and activity, and enhance the conductivity for OERs. This  $\text{CeO}_2/\text{Bi}_2\text{WO}_6$  consists of the heterojunction engineering that can open a modern method of thinking for high effective OER electrocatalysts.

 Received 28th December 2022  
 Accepted 26th February 2023

DOI: 10.1039/d2ra08273j

[rsc.li/rsc-advances](http://rsc.li/rsc-advances)

## 1. Introduction

The energy demands and increasing environmental problem lead to a lot of research efforts in studying exchangeable conversion system and energy storage.<sup>1–6</sup> The oxygen evolution reaction (OER) is key to the progress of renewable energy devices such as water-splitting devices and metal-air batteries.<sup>7–17</sup> At the anode, the even work of the OER depends on catalyst engineering owing to its essentially sluggish reaction kinetics and multielectron transfer paths.<sup>18–22</sup> Generally, noble metal oxides such as  $\text{IrO}_2$  and  $\text{RuO}_2$  are well-known electrocatalysts for OERs.<sup>23–27</sup> However, their high price, serious scarcity, and unsatisfied stability of electrocatalysts are greatly frustrating in that they are more widely applied to a variety of energy devices. Therefore, it is crucial to explore effective, low-cost, abundant, and robust OER catalysts on Earth.

One of the easiest members of the Aurivillius family, bismuth tungstate ( $\text{Bi}_2\text{WO}_6$ ) has become an outstanding OER electrocatalyst because of its abundant, low cost, clean properties, and excellent chemical stability.<sup>28–31</sup> In detail, two-

dimensional  $\text{Bi}_2\text{WO}_6$  nanosheets have a distinctive layer form and large specific surface area. These are useful to charge transfer, electrolyte penetration as well as active site exposure, regarded as a favorable catalyst support.<sup>32,33</sup> Nonetheless, by the self-aggregating motion,  $\text{Bi}_2\text{WO}_6$  nanosheets are simply aggregated to limit and decrease the electrochemically active region, indicating that the catalytic activity of OER is low.<sup>30</sup> According to the surface structure, the adsorption actions of reaction region and charge distribution are crucial to the electrochemical catalytic action.<sup>34</sup> Therefore, the interface engineering of heterostructures has been regarded as an effective strategy for optimizing the catalyst activities.<sup>35–40</sup> The close connections between different active species in engineering interfaces optimize the powerful synergistic effect, rapid charge transfer rate and activation energy, and adsorption for intermediates, overcoming the shortcomings of single ingredient materials,<sup>36–38</sup> whereas the heterointerfaces usually involve structural modification such as edges and dislocations as well as atomic defects including cation and anion vacancies, forming more active sites on the surface of the catalyst.<sup>41</sup> To accomplish this aim, it is essential to choose appropriate introduced species that form the optimal electrocatalysts. Due to its chemical properties and unique electronic structure,  $\text{CeO}_2$  has been extensively studied as an effective supporter of the OER. The abundant oxygen vacancies of  $\text{CeO}_2$  and flexible conversion between  $\text{Ce}^{3+}$  and  $\text{Ce}^{4+}$  can enable several moving oxygen atoms to access active sites as an oxygen buffer for the effective absorption of oxygen species.<sup>42–47</sup> Thus, we think that the hybridization of  $\text{Bi}_2\text{WO}_6$

<sup>a</sup>School of Chemical Engineering & Materials Science, Chung-Ang University, 84 Heukseok-ro, Dongjak-gu, Seoul, Korea. E-mail: [jooheonkim@cau.ac.kr](mailto:jooheonkim@cau.ac.kr)

<sup>b</sup>Department of Advanced Materials Engineering, Chung-Ang University, Anseong-si, Gyeonggi-do 17546, Republic of Korea

<sup>c</sup>Department of Intelligent Energy and Industry, Graduate School, Chung-Ang University, Seoul 06974, Republic of Korea

† Electronic supplementary information (ESI) available. See DOI: <https://doi.org/10.1039/d2ra08273j>



and  $\text{CeO}_2$  has to be a reasonable tactic to enhance the OER activity by the interface engineering.

In this work, we manufacture a modern sort of  $\text{CeO}_2/\text{Bi}_2\text{WO}_6$  heterostructure consisting of  $\text{CeO}_2$  nanoparticles on  $\text{Bi}_2\text{WO}_6$  nanosheets by a hydrothermal method for OER electrocatalysts in alkaline media. The excellent electrocatalytic active site and durability come from the distinct heterostructure and combined interface synergistic effect with equally distributed  $\text{CeO}_2$  nanoparticles fixing  $\text{Bi}_2\text{WO}_6$  nanosheets, which disclose more activity, have charge transfer rates, and show steady heterostructures. At the heterostructure, this approach *via* bonding the shape plan and electronic transformation fulfills advancement of catalysts, which supply direction for using activity encouraging and high effectiveness and stability OER electrocatalysts.

## 2. Experiment method

### 2.1. Synthesis of $\text{Bi}_2\text{WO}_6$ nanosheets

First, 0.05 g hexadecyltrimethylammonium bromide (CTAB) (0.1 mmol) was dispersed in 80 ml deionized water under stirring for 10 minutes. Then, 0.917 g  $\text{Bi}(\text{NO}_3)_3 \cdot 5\text{H}_2\text{O}$  was added to the obtained solution for 30 minutes. Finally, 0.33 g  $\text{Na}_2\text{WO}_4 \cdot 2\text{H}_2\text{O}$  was added to the solution and stirred for 30 minutes. Afterward, the as-obtained solution was transferred to a 100 ml Teflon-lined hydrothermal autoclave, which was then maintained at 120 °C for 24 hours. Finally, the precursor was washed several times with deionized water and dried at 50 °C overnight.

### 2.2. Synthesis of $\text{CeO}_2/\text{Bi}_2\text{WO}_6$ nanohybrids

First, 1 mmol  $\text{Ce}(\text{NH}_4)_2(\text{NO}_3)_6$  (0.5482 g) was added into 50 ml deionized water under a stirring process for 30 minutes. Then, 0.5 mmol  $\text{Bi}_2\text{WO}_6$  (0.3488 g) was added to this solution and ultrasonicated until complete dissolution. After sonication, 10 ml of  $\text{NaBH}_4$  solution (0.05 M) was added to the solution. The product was washed several times with ethanol and deionized water and dried at 50 °C overnight. After drying overnight, the as-prepared sample was calcined at 420 °C for 2 hours.

### 2.3. Synthesis of $\text{CeO}_2$ nanoparticles

The synthesis of  $\text{CeO}_2$  is similar to that of the  $\text{CeO}_2/\text{Bi}_2\text{WO}_6$  nanohybrid except for the additional treatment. To be more specific, although other experimental methods remain the same, only the second process of the  $\text{CeO}_2/\text{Bi}_2\text{WO}_6$  nanohybrid synthesis method was excluded.

## 3. Results and discussion

Fig. 1 describes the process of formation of  $\text{CeO}_2/\text{Bi}_2\text{WO}_6$  nanohybrids *via* a hydrothermal reaction. The first process began with use of hydrothermal synthesis of  $\text{Bi}_2\text{WO}_6$  nanosheets. The Br-ion CTAB bound on the  $\text{Bi}_2\text{WO}_6$  surface can adsorb positively charged  $\text{Ce}^{4+}$  ions.<sup>31,48</sup> Next,  $\text{Ce}^{4+}$  ions were easily reduced to  $\text{CeO}_2$  nanoparticles by forming nanohybrids of  $\text{CeO}_2/\text{Bi}_2\text{WO}_6$  using  $\text{NaBH}_4$  as a reducing agent accumulated on the  $\text{Bi}_2\text{WO}_6$  nanosheet.<sup>31</sup> During the experiment, Bi-ions and W-

ions could be reduced by  $\text{NaBH}_4$  that obtains the advantages of Bi–O–Ce, W–O–Ce bond formation by substituting Br– to Ce–O–. The  $\text{CeO}_2/\text{Bi}_2\text{WO}_6$  nanohybrid was annealed at 420 °C in air, and thus, stable fixed  $\text{CeO}_2$  nanoparticles were bonded to the  $\text{Bi}_2\text{WO}_6$  surface. The  $\text{NaBH}_4$  reduction was selected because it is easy to perform and inexpensive for the manufacture of vacancies. In addition, it generates many defects for exposing more reactive sites and increases the conductivity.<sup>49</sup>

### 3.1. Morphology and structure of $\text{CeO}_2/\text{Bi}_2\text{WO}_6$

The morphology and microstructure of the prepared samples were analyzed by FE-SEM, as shown in Fig. S1, S2<sup>†</sup> and 2. As shown in Fig. S1a and b (ESI<sup>†</sup>), the microstructure of the  $\text{CeO}_2$  sample was characterized by nanoparticles. The morphology of  $\text{Bi}_2\text{WO}_6$  showed nanosheet features, as shown in Fig. S2a and b (ESI<sup>†</sup>). After addition of  $\text{NaBH}_4$  and  $\text{Ce}(\text{NH}_4)_2(\text{NO}_3)_6$  and calcination at 420 °C for 2 hours,  $\text{CeO}_2/\text{Bi}_2\text{WO}_6$  could not change the structure of  $\text{Bi}_2\text{WO}_6$  nanosheets (Fig. 2), which implies that the microstructure of  $\text{Bi}_2\text{WO}_6$  could be maintained by the addition of  $\text{NaBH}_4$  and  $\text{Ce}(\text{NH}_4)_2(\text{NO}_3)_6$  and calcination could keep the microstructure of  $\text{Bi}_2\text{WO}_6$ . In addition, the surface nanoparticles cannot be found on the  $\text{CeO}_2/\text{Bi}_2\text{WO}_6$  nanohybrid due to the low loading and uniform growth on the  $\text{Bi}_2\text{WO}_6$  nanosheet of  $\text{CeO}_2$  nanoparticles.<sup>28,29</sup> Meanwhile, the irregular nanoparticles on the surface could be distinguished from the surface of the  $\text{Bi}_2\text{WO}_6$  nanosheets. This suggests that the  $\text{CeO}_2$  nanoparticles were successfully fixed and uniformly grown on the  $\text{Bi}_2\text{WO}_6$  nanosheets. The distinctive heterostructure provided strong electron interaction and interfacial synergy between  $\text{Bi}_2\text{WO}_6$  nanosheets and  $\text{CeO}_2$  nanoparticles, which is important for adjusting the electronic structure and exposing several active sites to increase the electrocatalytic activity and durability of electrocatalysts.<sup>50,51</sup>

To further examine the structure of  $\text{CeO}_2$  nanoparticles on the surface of  $\text{Bi}_2\text{WO}_6$  nanosheets, the crystal structure of  $\text{CeO}_2$ ,  $\text{Bi}_2\text{WO}_6$ , and  $\text{CeO}_2/\text{Bi}_2\text{WO}_6$  was investigated by FE-TEM analysis, as shown in Fig. S3, S4<sup>†</sup> and 3. As illustrated in Fig. S3a and b,<sup>†</sup> the FE-TEM images displayed  $\text{CeO}_2$  with nanoparticle structure, implying that the  $\text{CeO}_2$  nanoparticles were synthesized. The HRTEM image of  $\text{CeO}_2$  indicated that the *d*-spacing of the lattice fringes is 0.271 and 0.312 nm, corresponding to the (200) and (111) planes, respectively, as shown in Fig. S3c<sup>†</sup>.<sup>52</sup> Meanwhile, the FE-TEM images represented  $\text{Bi}_2\text{WO}_6$  with a sheet-like form, and the nanosheets can be seen in Fig. S4a and b,<sup>†</sup> showing that  $\text{Bi}_2\text{WO}_6$  nanosheets were synthesized. As shown in Fig. S4c,<sup>†</sup> the HRTEM image shows that the *d*-space of lattice fringes is 0.272 nm, corresponding to the (020) plane of

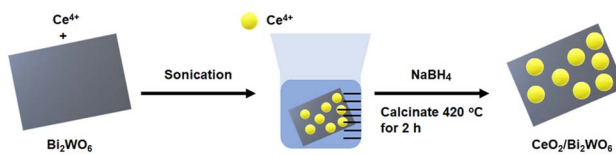


Fig. 1 Schematic illustration of synthesis process of  $\text{CeO}_2/\text{Bi}_2\text{WO}_6$  nanohybrids.



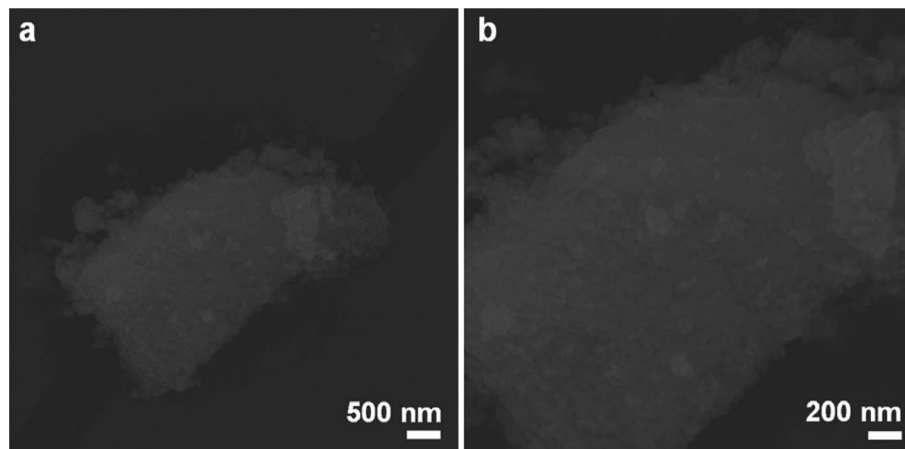


Fig. 2 FE-SEM images at (a) low magnification and (b) high magnification of  $\text{CeO}_2/\text{Bi}_2\text{WO}_6$  nanohybrids.

$\text{Bi}_2\text{WO}_6$ .<sup>53</sup> The FE-TEM images of  $\text{CeO}_2/\text{Bi}_2\text{WO}_6$  nanohybrids are displayed in Fig. 3a and b. The  $\text{CeO}_2/\text{Bi}_2\text{WO}_6$  sample was large and had nanosheet properties, and irregular  $\text{CeO}_2$  nanoparticles were dispersed on the  $\text{Bi}_2\text{WO}_6$  nanosheets. In addition, it could be found that some nanoparticles were spread out on the  $\text{Bi}_2\text{WO}_6$  nanosheets, confirming that the  $\text{CeO}_2$  nanoparticles were grown on the  $\text{Bi}_2\text{WO}_6$  nanosheets, which is consistent with the FE-SEM results.<sup>54</sup> Fig. 3c shows the HRTEM image of the  $\text{CeO}_2/\text{Bi}_2\text{WO}_6$  nanohybrid catalyst, and the lattice edges of  $\text{CeO}_2$  nanoparticles and  $\text{Bi}_2\text{WO}_6$  nanosheets might be surely differentiated, and the lattice edges of 0.271 nm, 0.312 nm, and 0.272 nm corresponded to the (200) and (101) planes of  $\text{CeO}_2$  and the (020) plane of  $\text{Bi}_2\text{WO}_6$ , respectively. Finally, to investigate the elemental composition of  $\text{CeO}_2/\text{Bi}_2\text{WO}_6$  nanohybrids catalyst, the energy dispersive X-ray

spectrometry (EDS) was perfected in Fig. 3e. The four elements of Ce, Bi, W, and O were uniformly distributed over the whole  $\text{CeO}_2/\text{Bi}_2\text{WO}_6$  nanohybrid catalyst, which suggested that the  $\text{CeO}_2$  nanoparticles combined with the surface of  $\text{Bi}_2\text{WO}_6$  nanosheets, confirming that the  $\text{CeO}_2$  nanoparticle/ $\text{Bi}_2\text{WO}_6$  nanosheet heterostructure was successfully synthesized.

To confirm the crystal structure and phase composition of  $\text{CeO}_2/\text{Bi}_2\text{WO}_6$ ,  $\text{CeO}_2$ , and  $\text{Bi}_2\text{WO}_6$  catalysts, we conducted X-ray diffraction (XRD), as shown in Fig. 4a. The peaks at  $28.7^\circ$ ,  $33.3^\circ$ ,  $47.6^\circ$ ,  $56.5^\circ$ ,  $59.3^\circ$ , and  $69.5^\circ$  corresponded to the (111), (200), (220), (311), (222), and (400) planes of  $\text{CeO}_2$ , respectively. These results were consistent with the  $\text{CeO}_2$  crystal structure (JCPDS No. 81-0792).<sup>55</sup> Similarly, the diffraction peaks of  $\text{CeO}_2/\text{Bi}_2\text{WO}_6$  and  $\text{Bi}_2\text{WO}_6$  matched JCPDS No. 73-2020 of  $\text{Bi}_2\text{WO}_6$ .<sup>56</sup> In addition, no diffraction peaks were studied from other materials.

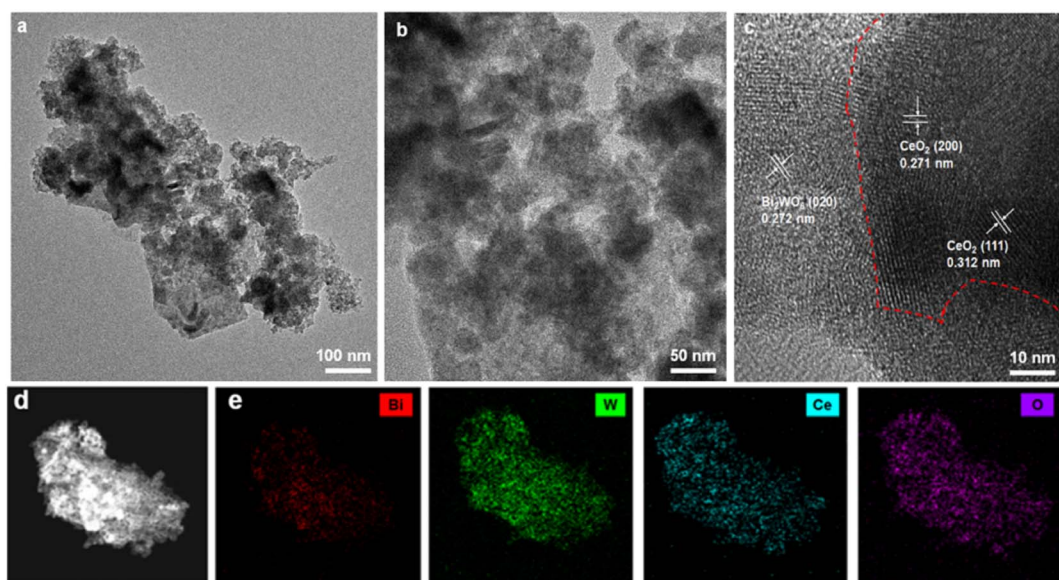


Fig. 3 FE-TEM images at (a) low magnification and (b) high magnification of  $\text{CeO}_2/\text{Bi}_2\text{WO}_6$  nanohybrids. (c) HRTEM image of  $\text{CeO}_2/\text{Bi}_2\text{WO}_6$  nanohybrids. (d) Dark-field FE-TEM image of  $\text{CeO}_2/\text{Bi}_2\text{WO}_6$  nanohybrids. (e) EDS mapping images for Bi, W, Ce, and O elements distributed at  $\text{CeO}_2/\text{Bi}_2\text{WO}_6$  nanohybrids.



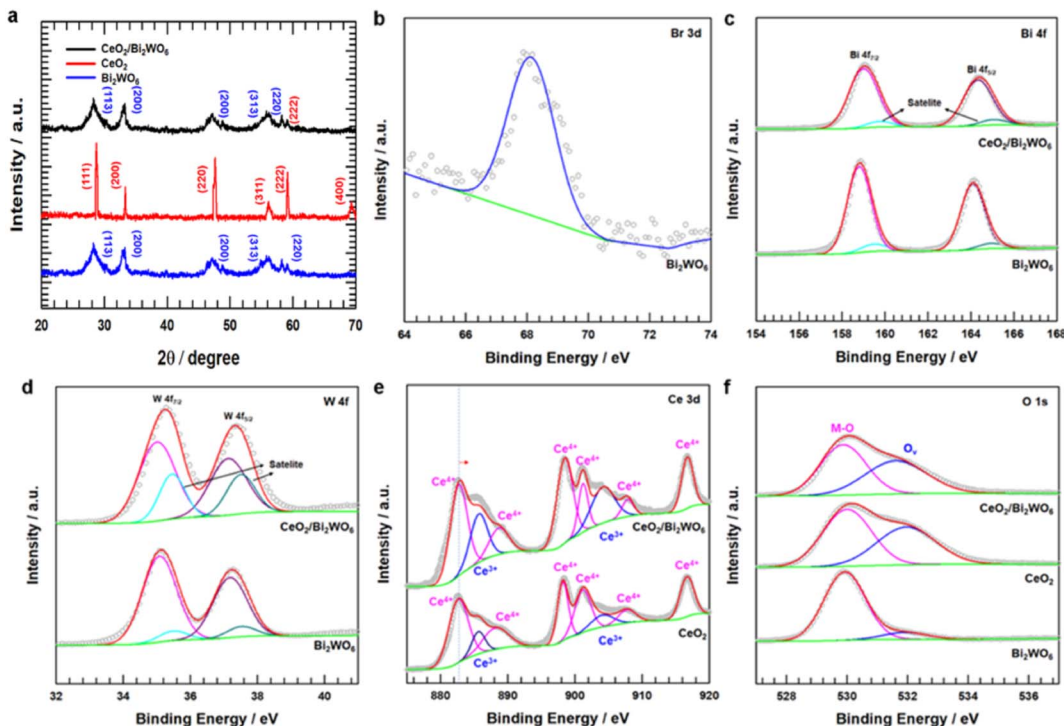


Fig. 4 (a) XRD pattern of  $\text{CeO}_2/\text{Bi}_2\text{WO}_6$ , and  $\text{CeO}_2/\text{Bi}_2\text{WO}_6$ . (b) XPS Br 3d deconvolution spectrum of  $\text{Bi}_2\text{WO}_6$ . (c) XPS Bi 4f deconvolution spectrum of  $\text{Bi}_2\text{WO}_6$  and  $\text{CeO}_2/\text{Bi}_2\text{WO}_6$ . (d) XPS W 4f deconvolution spectrum of  $\text{Bi}_2\text{WO}_6$  and  $\text{CeO}_2/\text{Bi}_2\text{WO}_6$ . (e) XPS Ce 3d deconvolution spectrum of  $\text{CeO}_2$  and  $\text{CeO}_2/\text{Bi}_2\text{WO}_6$ . (f) XPS O 1s deconvolution spectrum of  $\text{CeO}_2$ ,  $\text{Bi}_2\text{WO}_6$  and  $\text{CeO}_2/\text{Bi}_2\text{WO}_6$ .

This might be the surface of the  $\text{Bi}_2\text{WO}_6$  nanosheets of the  $\text{CeO}_2$  nanoparticles due to low loading and even growth.<sup>29–31</sup>

To identify the chemical valence states and surface elemental contents, the X-ray photoelectron (XPS) spectra recorded for  $\text{CeO}_2$ ,  $\text{Bi}_2\text{WO}_6$ , and  $\text{CeO}_2/\text{Bi}_2\text{WO}_6$  are shown in Fig. S5† and 4b–f. As shown in Fig. S5,† the XPS survey spectrum indicated the existence of Ce, Bi, W, and O elements, in accordance with the above-mentioned XRD result (Fig. 4a). Fig. 4b–f displays the high-resolution spectra of Br 3d, Bi 4f, W 4f, Ce 3d and O 1s, respectively. In the case of pure  $\text{Bi}_2\text{WO}_6$ , the binding energies of the Br 3d peak were determined to be 68.6 eV, as shown in Fig. 4b, confirming that the Br ions of CTAB were bound to the surface Bi and W atoms of  $\text{Bi}_2\text{WO}_6$ .<sup>53</sup> As shown in

Fig. 4c,  $\text{Bi}_2\text{WO}_6$  and  $\text{CeO}_2/\text{Bi}_2\text{WO}_6$  could be divided into two Bi 4f peaks. The properties of  $\text{Bi} 4f_{5/2}$  and  $\text{Bi} 4f_{7/2}$  were two peaks at 164.3 and 159.2 eV that matched  $\text{Bi}^{3+}$  ions of  $\text{Bi}_2\text{WO}_6$ .<sup>57</sup> The shoulder peaks  $\text{Bi} 4f_{5/2}$  and  $\text{Bi} 4f_{7/2}$ , corresponding to 165.6 and 160.6 eV, appeared at a higher binding energy. The peaks of Bi, represented at a higher energy, meant that the Bi atoms had higher electrical positivity in binding with the surface Br atoms.<sup>53,57</sup> Similarly, for the high-resolution XPS W 4f spectrum (Fig. 4d),  $4f_{7/2}$  and  $4f_{5/2}$  electron orbits of  $\text{W}^{6+}$  corresponded to two feature peaks at 35.2 eV and 37.3 eV, respectively. In addition, the orbits of  $\text{W} 4f_{7/2}$  and  $4f_{5/2}$  belonged to the satellite peaks at 35.6 eV and 37.6 eV, respectively. Compared to  $\text{Bi}_2\text{WO}_6$ , the binding energy of  $\text{CeO}_2/\text{Bi}_2\text{WO}_6$  was moved slightly to the

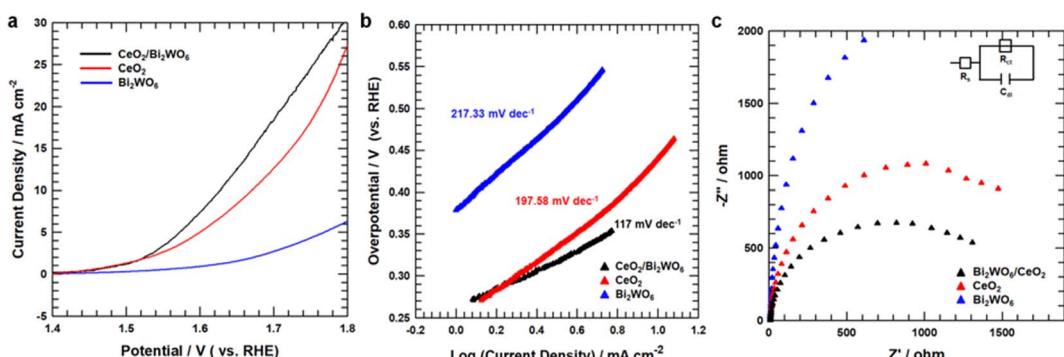


Fig. 5 (a) OER LSV curves for  $\text{CeO}_2$ ,  $\text{Bi}_2\text{WO}_6$ , and  $\text{CeO}_2/\text{Bi}_2\text{WO}_6$  in a  $\text{N}_2$ -saturated 1.0 M KOH electrolyte. (b) Tafel plots for  $\text{CeO}_2$ ,  $\text{Bi}_2\text{WO}_6$ , and  $\text{CeO}_2/\text{Bi}_2\text{WO}_6$ . (c) Nyquist plots for  $\text{CeO}_2$ ,  $\text{Bi}_2\text{WO}_6$ , and  $\text{CeO}_2/\text{Bi}_2\text{WO}_6$  recorded at 1.65 V.



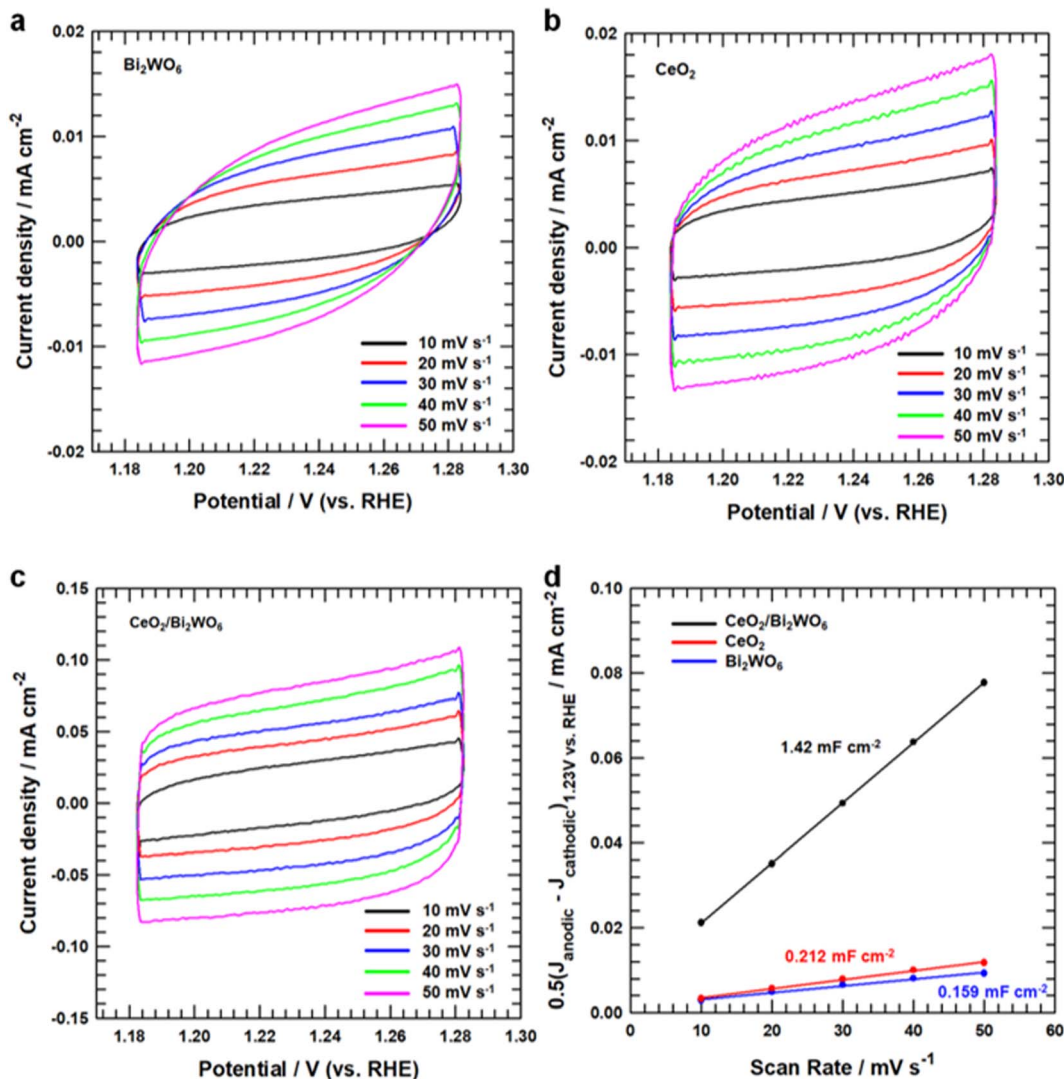


Fig. 6 CV curves (a)  $\text{CeO}_2$ , (b)  $\text{Bi}_2\text{WO}_6$ , and (c)  $\text{CeO}_2/\text{Bi}_2\text{WO}_6$  in a non-faradaic current region (1.18–1.28 V vs. RHE) at different scan rates of 10, 20, 30, 40, and 50 mV s<sup>-1</sup>. (d) Linear fitting of the capacitive currents versus CV scan rates of  $\text{CeO}_2$ ,  $\text{Bi}_2\text{WO}_6$ , and  $\text{CeO}_2/\text{Bi}_2\text{WO}_6$ .

negative parts, confirming that the electropositive W appearing on the  $\text{Bi}_2\text{WO}_6$  nanosheets was increasingly higher.<sup>28,53</sup> The high-resolution XPS Ce 3d spectrum for  $\text{CeO}_2/\text{Bi}_2\text{WO}_6$  was composed with the peaks compared to  $\text{CeO}_2$  (Fig. 4e). The Ce 3d spectrum of  $\text{CeO}_2/\text{Bi}_2\text{WO}_6$  and  $\text{CeO}_2$  samples could be separated into eight peaks, two peaks were assigned to  $\text{Ce}^{3+}$  at 885.7 and 904.2 eV, and six peaks were assigned to  $\text{Ce}^{4+}$  at 882.7, 888.7, 898.5, 901.2, 907.9, and 916.7 eV for  $\text{CeO}_2/\text{Bi}_2\text{WO}_6$ .<sup>58</sup> According to the Ce 3d spectrum analysis,  $\text{Ce}^{3+}$  and  $\text{Ce}^{4+}$  were present in  $\text{CeO}_2$  and  $\text{CeO}_2/\text{Bi}_2\text{WO}_6$ . For the Ce 3d spectrum, it might be observed that  $\text{CeO}_2$  and  $\text{CeO}_2/\text{Bi}_2\text{WO}_6$  were plentiful in  $\text{Ce}^{3+}$  species, which showed the formation of oxygen vacancies in these two samples.<sup>58</sup> Besides, the binding energy of the Ce 3d spectrum in  $\text{CeO}_2/\text{Bi}_2\text{WO}_6$  had a clear positive change compared to  $\text{CeO}_2$ . The suitable electron structure of  $\text{CeO}_2/\text{Bi}_2\text{WO}_6$  could help to enhance the catalyst's OER performance by inducing charge redistribution at the interface.<sup>59,60</sup> Fig. 4f shows the two peaks for the O 1s spectrum. The O 1s peak at

530.2 eV was attributed to the oxygen atom bonded to the metal, and the center position at 532.1 eV was ascribed to the oxygen atom in the surrounding area of oxygen vacancies.<sup>61</sup> However, according to the feature peak, the peak area at 532.1 eV varied greatly, which displayed that the  $\text{CeO}_2/\text{Bi}_2\text{WO}_6$  nanohybrids had much more oxygen vacancies. Interestingly, as shown in Table S1,<sup>†</sup> the  $\text{CeO}_2/\text{Bi}_2\text{WO}_6$  nanohybrids (46.8%) is higher than that of  $\text{CeO}_2$  nanoparticles (44.6%) and  $\text{Bi}_2\text{WO}_6$  nanosheets (9.7%). These results indicated that the  $\text{CeO}_2/\text{Bi}_2\text{WO}_6$  nanohybrids had enough oxygen vacancies. As a result, the  $\text{CeO}_2$  nanoparticles abundant in evenly grown oxygen vacancies on  $\text{Bi}_2\text{WO}_6$  nanosheets were successfully synthesized.

### 3.2. Oxygen electrochemical performance of electrocatalysts

To study the OER catalytic active sites of all samples, we studied the electrochemical characteristics of  $\text{CeO}_2/\text{Bi}_2\text{WO}_6$ ,  $\text{CeO}_2$ , and  $\text{Bi}_2\text{WO}_6$  for OERs in alkaline solutions (pH = 14) using a rotating disk electrode (RDE) (see Detail Methods in the ESI<sup>†</sup>).

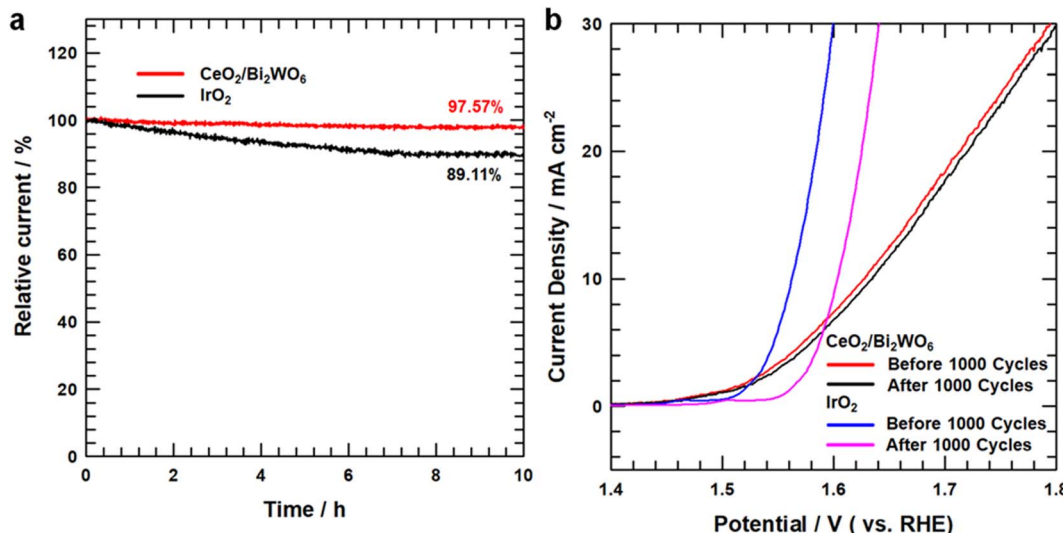


Fig. 7 (a) OER chronoamperometry test of CeO<sub>2</sub>/Bi<sub>2</sub>WO<sub>6</sub> and IrO<sub>2</sub>. (b) OER LSV curves for before and after 1000 cycles CeO<sub>2</sub>/Bi<sub>2</sub>WO<sub>6</sub> and IrO<sub>2</sub>.

As shown in Fig. 5a, the linear sweep voltammetry (LSV) curves showed that CeO<sub>2</sub>/Bi<sub>2</sub>WO<sub>6</sub> indicated a smaller overpotential of 390 mV, slightly larger than that of CeO<sub>2</sub> (440 mV) and Bi<sub>2</sub>WO<sub>6</sub>. Besides, to evidence the outstanding OER kinetics of the samples, their Tafel slope were calculated by LSV. As shown in Fig. 5b, CeO<sub>2</sub>/Bi<sub>2</sub>WO<sub>6</sub> showed a lower Tafel slope (117 mV dec<sup>-1</sup>) than that of CeO<sub>2</sub> (197.58 mV dec<sup>-1</sup>) and Bi<sub>2</sub>WO<sub>6</sub> (217.33 mV dec<sup>-1</sup>), and thus CeO<sub>2</sub>/Bi<sub>2</sub>WO<sub>6</sub> had the fastest kinetic process.<sup>62,63</sup> Compared with previous studies, the CeO<sub>2</sub>/Bi<sub>2</sub>WO<sub>6</sub> heterostructure was one of the most efficient Bi<sub>2</sub>WO<sub>6</sub>-based catalysts (Table S2†). The smallest Tafel slope of CeO<sub>2</sub>/Bi<sub>2</sub>WO<sub>6</sub> suggested the most favorable OER kinetics, indicating that CeO<sub>2</sub>/Bi<sub>2</sub>WO<sub>6</sub> possessed an outstanding OER catalytic kinetics. To investigate the OER kinetics of CeO<sub>2</sub>/Bi<sub>2</sub>WO<sub>6</sub>, CeO<sub>2</sub>, and Bi<sub>2</sub>WO<sub>6</sub>, electrochemical impedance spectroscopy (EIS) was conducted, as shown in Fig. 5c. The CeO<sub>2</sub>/Bi<sub>2</sub>WO<sub>6</sub> nanohybrids had the lowest charge resistance ( $R_{ct}$ ) than other samples at the interface between the electrolyte and the catalyst. Since  $R_{ct}$  represented the rate of charge transfer in OERs,<sup>64</sup> the smallest  $R_{ct}$  value of the CeO<sub>2</sub>/Bi<sub>2</sub>WO<sub>6</sub> nanohybrid showed the high-speed electron transportation ability of the CeO<sub>2</sub>/Bi<sub>2</sub>WO<sub>6</sub> nanohybrid during the OER process due to the CeO<sub>2</sub> nanoparticles plentiful in oxygen vacancies evenly grown on Bi<sub>2</sub>WO<sub>6</sub> nanosheets.<sup>28</sup>

To establish why CeO<sub>2</sub>/Bi<sub>2</sub>WO<sub>6</sub> had better OER activity than that of other samples, we measured double-layer capacitance ( $C_{dl}$ ) to judge their electrochemically active surface area (ECSA). The ECSA of CeO<sub>2</sub>/Bi<sub>2</sub>WO<sub>6</sub>, CeO<sub>2</sub>, and Bi<sub>2</sub>WO<sub>6</sub> was revealed by a cyclic voltammetry (CV) method.<sup>65–67</sup> Fig. 6a–c display the CV curves at different scan rates (10–50 mV s<sup>-1</sup>) for CeO<sub>2</sub>/Bi<sub>2</sub>WO<sub>6</sub>, CeO<sub>2</sub>, and Bi<sub>2</sub>WO<sub>6</sub> alkaline solutions, respectively. As the scan speed increased, the current densities of CeO<sub>2</sub>/Bi<sub>2</sub>WO<sub>6</sub>, CeO<sub>2</sub>, and Bi<sub>2</sub>WO<sub>6</sub> increased accordingly, indicating that the active sites and charge transport capability of CeO<sub>2</sub>/Bi<sub>2</sub>WO<sub>6</sub>, CeO<sub>2</sub>, and Bi<sub>2</sub>WO<sub>6</sub> increased significantly. In addition, it displayed that CeO<sub>2</sub>/Bi<sub>2</sub>WO<sub>6</sub> showed the highest capacitive current

compared with CeO<sub>2</sub> and Bi<sub>2</sub>WO<sub>6</sub>. The  $C_{dl}$  and ECSA can be calculated as “ $0.5(J_{\text{anodic}}-J_{\text{cathodic}})_{1.23} \text{ V vs. RHE}$  (mA cm<sup>-2</sup>)/scan rate (mV s<sup>-1</sup>)”, as shown in Fig. 6d, and the  $C_{dl}$  of CeO<sub>2</sub>/Bi<sub>2</sub>WO<sub>6</sub> (1.42 mF cm<sup>-2</sup>) is remarkably higher than that of CeO<sub>2</sub> (0.212 mF cm<sup>-2</sup>) and Bi<sub>2</sub>WO<sub>6</sub> (0.159 mF cm<sup>-2</sup>). As a result, the significant activities of  $C_{dl}$  and ECSA increased, which might be due to the high oxygen vacancy concentration of the CeO<sub>2</sub>/Bi<sub>2</sub>WO<sub>6</sub> heterostructure, and CeO<sub>2</sub> nanoparticles equally grown on Bi<sub>2</sub>WO<sub>6</sub>, which essentially improved the electrocatalytic activity.

The electrocatalytic stability of the CeO<sub>2</sub>/Bi<sub>2</sub>WO<sub>6</sub> nanohybrids and IrO<sub>2</sub> was tested by chronoamperometry measurements, as shown in Fig. 7a, and the current density of CeO<sub>2</sub>/Bi<sub>2</sub>WO<sub>6</sub> indicated the unseen modification with respect to the initial value at a retention rate of up to 97.57% after 10 hours of the OER process and showed outstanding stability in an aqueous alkaline medium. In IrO<sub>2</sub>, the current retention rate is below 89.11%. Besides, the durability of CeO<sub>2</sub>/Bi<sub>2</sub>WO<sub>6</sub> was performed by the LSV curves before and after 1000 cycles of the CV curves. As shown in Fig. 7b, the CeO<sub>2</sub>/Bi<sub>2</sub>WO<sub>6</sub> electrocatalyst showed a negligible decrease in current density, suggesting the good durability of CeO<sub>2</sub>/Bi<sub>2</sub>WO<sub>6</sub> in alkaline solutions, while IrO<sub>2</sub> shows a significant decrease after 1000 cycles. Because of the synergistic effect of highly stable heterojunctions, the Bi<sub>2</sub>WO<sub>6</sub> nanosheets not only guarantee rich active sites, but also ensure a variety of paths for the fast and efficient movement of electrolytes and gases. Meanwhile, the reasonably fixed CeO<sub>2</sub> nanoparticles increase the electrocatalytic activity and enhance the electrical contact with the electrolyte.<sup>68,69</sup> The above-mentioned electrochemical results confirmed the presence of more active sites, and more efficient and faster electron transport capability in CeO<sub>2</sub>/Bi<sub>2</sub>WO<sub>6</sub> than those in samples of CeO<sub>2</sub> and Bi<sub>2</sub>WO<sub>6</sub>, confirming that the CeO<sub>2</sub>/Bi<sub>2</sub>WO<sub>6</sub> heterostructure catalyst had fine catalytic activity and maintained the excellent stability in an alkaline environment. Therefore, the CeO<sub>2</sub>/Bi<sub>2</sub>WO<sub>6</sub> heterostructure catalyst is a reasonable strategy to



optimize the OER active sites and durability of  $\text{Bi}_2\text{WO}_6$ -based catalysts.

## 4. Conclusion

In summary, we have developed a simple strategy to synthesize  $\text{CeO}_2/\text{Bi}_2\text{WO}_6$  nanohybrids with more OER active sites and high durability under alkaline conditions. The characterization and electrochemical measurement results indicated that the  $\text{CeO}_2/\text{Bi}_2\text{WO}_6$  heterostructure electrocatalyst displayed not only more OER catalytic active sites with a smaller overpotential of 390 mV and a lower Tafel slope of 117 mV  $\text{dec}^{-1}$  but also durability for 12 h. The distinct heterointerface generates hard bonded electronic effects and the interfacial synergistic effect, making the  $\text{CeO}_2$  nanoparticles uniformly anchored onto  $\text{Bi}_2\text{WO}_6$  for the atoms to expose more active sites, which provided  $\text{CeO}_2/\text{Bi}_2\text{WO}_6$  with electrocatalytic active sites for OERs. Meanwhile, the hard coupled and interfacial synergistic effect really endows the heterojunction structure with good stability for practical application. This  $\text{CeO}_2/\text{Bi}_2\text{WO}_6$  heterostructure catalyst has been developed *via* shape design.

## Conflicts of interest

There are no conflicts to declare.

## Acknowledgements

This research was supported by the Chung-Ang University Research Scholarship Grants in 2023 and also supported by the National Research Foundation of Korea (NRF) grant funded by the Korea government (MSIT) (2020R1A2C2010445).

## References

1. J. Chen, X. J. Wu, L. Yin, B. Li, X. Hong, Z. Fan, B. Chen, C. Xue and H. Zhang, One-pot synthesis of CdS nanocrystals hybridized with single-layer transition-metal dichalcogenide nanosheets for efficient photocatalytic hydrogen evolution, *Angew. Chem., Int. Ed. Engl.*, 2015, **54**, 1210–1214.
2. P. Chen, K. Xu, S. Tao, T. Zhou, Y. Tong, H. Ding, L. Zhang, W. Chu, C. Wu and Y. Xie, Phase-Transformation Engineering in Cobalt Diselenide Realizing Enhanced Catalytic Activity for Hydrogen Evolution in an Alkaline Medium, *Adv. Mater.*, 2016, **28**, 7527–7532.
3. Z. W. Seh, J. Kibsgaard, C. F. Dickens, I. Chorkendorff, J. K. Norskov and T. F. Jaramillo, Combining theory and experiment in electrocatalysis: Insights into materials design, *Science*, 2017, **355**, 146.
4. Q. Song, J. Li, L. Wang, Y. Qin, L. Pang and H. Liu, Stable single-atom cobalt as a strong coupling bridge to promote electron transfer and separation in photoelectrocatalysis, *J. Catal.*, 2019, **370**, 176–185.
5. S. Sultan, J. N. Tiwari, A. N. Singh, S. Zhumagali, M. Ha, C. W. Myung, P. Thangavel and K. S. Kim, Single Atoms and Clusters Based Nanomaterials for Hydrogen Evolution, Oxygen Evolution Reactions, and Full Water Splitting, *Adv. Energy Mater.*, 2019, **9**, 1900624.
6. X. Zou and Y. Zhang, Noble metal-free hydrogen evolution catalysts for water splitting, *Chem. Soc. Rev.*, 2015, **44**, 5148–5180.
7. D. Dong, Z. Wu, J. Wang, G. Fu and Y. Tang, Recent progress in Co9S8-based materials for hydrogen and oxygen electrocatalysis, *J. Mater. Chem. A*, 2019, **7**, 16068–16088.
8. G. Fu, X. Jiang, Y. Chen, L. Xu, D. Sun, J.-M. Lee and Y. Tang, Robust bifunctional oxygen electrocatalyst with a “rigid and flexible” structure for air-cathodes, *NPG Asia Mater.*, 2018, **10**, 618–629.
9. G. Fu, Y. Tang and J.-M. Lee, Recent Advances in Carbon-Based Bifunctional Oxygen Electrocatalysts for Zn–Air Batteries, *ChemElectroChem*, 2018, **5**, 1424–1434.
10. F. Lyu, Q. Wang, S. M. Choi and Y. Yin, Noble-Metal-Free Electrocatalysts for Oxygen Evolution, *Small*, 2019, **15**, 1804201.
11. N. T. Suen, S. F. Hung, Q. Quan, N. Zhang, Y. J. Xu and H. M. Chen, Electrocatalysis for the oxygen evolution reaction: recent development and future perspectives, *Chem. Soc. Rev.*, 2017, **46**, 337–365.
12. M. Tahir, L. Pan, F. Idrees, X. Zhang, L. Wang, J.-J. Zou and Z. L. Wang, Electrocatalytic oxygen evolution reaction for energy conversion and storage: A comprehensive review, *Nano Energy*, 2017, **37**, 136–157.
13. P. Tan, B. Chen, H. Xu, W. Cai, W. He and M. Ni, In-situ growth of Co3O4 nanowire-assembled clusters on nickel foam for aqueous rechargeable Zn-Co3O4 and Zn-air batteries, *Appl. Catal., B*, 2019, **241**, 104–112.
14. N. K. Wagh, S. S. Shinde, C. H. Lee, J.-Y. Jung, D.-H. Kim, S.-H. Kim, C. Lin, S. U. Lee and J.-H. Lee, Densely colonized isolated Cu-N single sites for efficient bifunctional electrocatalysts and rechargeable advanced Zn-air batteries, *Appl. Catal., B*, 2020, **268**, 118746.
15. Q. Zhao, N. Katyal, I. D. Seymour, G. Henkelman and T. Ma, Vanadium(III) Acetylacetone as an Efficient Soluble Catalyst for Lithium-Oxygen Batteries, *Angew. Chem., Int. Ed.*, 2019, **58**, 12553–12557.
16. X. Zheng, J. Wu, X. Cao, J. Abbott, C. Jin, H. Wang, P. Strasser, R. Yang, X. Chen and G. Wu, N-, P-, and S-doped graphene-like carbon catalysts derived from onium salts with enhanced oxygen chemisorption for Zn-air battery cathodes, *Appl. Catal., B*, 2019, **241**, 442–451.
17. J. Sun, H. Xue, Y. Zhang, X. L. Zhang, N. Guo, T. Song, H. Dong, Y. Kong, J. Zhang and Q. Wang, Unraveling the Synergistic Effect of Heteroatomic Substitution and Vacancy Engineering in CoFe2O4 for Superior Electrocatalysis Performance, *Nano Lett.*, 2022, **22**, 3503–3511.
18. D. K. Bediako, B. Lassalle-Kaiser, Y. Surendranath, J. Yano, V. K. Yachandra and D. G. Nocera, Structure-activity correlations in a nickel-borate oxygen evolution catalyst, *J. Am. Chem. Soc.*, 2012, **134**, 6801–6809.
19. P. Chen, K. Xu, T. Zhou, Y. Tong, J. Wu, H. Cheng, X. Lu, H. Ding, C. Wu and Y. Xie, Strong-Coupled Cobalt Borate Nanosheets/Graphene Hybrid as Electrocatalyst for Water



Oxidation Under Both Alkaline and Neutral Conditions, *Angew. Chem., Int. Ed.*, 2016, **55**, 2488–2492.

20 Q. Shi, C. Zhu, D. Du and Y. Lin, Robust noble metal-based electrocatalysts for oxygen evolution reaction, *Chem. Soc. Rev.*, 2019, **48**, 3181–3192.

21 R. Subbaraman, D. Tripkovic, K. C. Chang, D. Strmcnik, A. P. Paulikas, P. Hirunsit, M. Chan, J. Greeley, V. Stamenkovic and N. M. Markovic, Trends in activity for the water electrolyser reactions on 3d M(Ni,Co,Fe,Mn) hydr(oxy)oxide catalysts, *Nat. Mater.*, 2012, **11**, 550–557.

22 B. Y. Xia, Y. Yan, N. Li, H. B. Wu, X. W. Lou and X. Wang, A metal–organic framework-derived bifunctional oxygen electrocatalyst, *Nat. Energy*, 2016, **1**, 15006.

23 J. Chen, C. Fan, X. Hu, C. Wang, Z. Huang, G. Fu, J. M. Lee and Y. Tang, Hierarchically Porous Co/Cox My (M = P, N) as an Efficient Mott-Schottky Electrocatalyst for Oxygen Evolution in Rechargeable Zn-Air Batteries, *Small*, 2019, **15**, 1901518.

24 K. Zhang, X. Xia, S. Deng, Y. Zhong, D. Xie, G. Pan, J. Wu, Q. Liu, X. Wang and J. Tu, Nitrogen-Doped Sponge Ni Fibers as Highly Efficient Electrocatalysts for Oxygen Evolution Reaction, *Nano-Micro Lett.*, 2019, **11**, 21.

25 R. Zhang, Y.-C. Zhang, L. Pan, G.-Q. Shen, N. Mahmood, Y.-H. Ma, Y. Shi, W. Jia, L. Wang, X. Zhang, W. Xu and J.-J. Zou, Engineering Cobalt Defects in Cobalt Oxide for Highly Efficient Electrocatalytic Oxygen Evolution, *ACS Catal.*, 2018, **8**, 3803–3811.

26 J. Sun, N. Guo, T. Song, Y.-R. Hao, J. Sun, H. Xue and Q. Wang, Revealing the interfacial electron modulation effect of CoFe alloys with CoC encapsulated in N-doped CNTs for superior oxygen reduction, *Adv. Powder Technol.*, 2022, **1**, 100023.

27 J. Sun, H. Xue, N. Guo, T. Song, Y. R. Hao, J. Sun, J. Zhang and Q. Wang, Synergetic Metal Defect and Surface Chemical Reconstruction into NiCo2S4/ZnS Heterojunction to Achieve Outstanding Oxygen Evolution Performance, *Angew. Chem., Int. Ed. Engl.*, 2021, **60**, 19435–19441.

28 J. Li, Z. Liang, Q. Song and X. Xu, Strong-coupled CoOx nanoparticles/Bi2WO6 nanosheets hybrid as electrocatalyst for water oxidation under alkaline conditions, *Mater. Res. Bull.*, 2019, **113**, 152–160.

29 J. Li, Z. Liang, Q. Song and X. Xu, NiFeOx nanosheets tight-coupled with Bi2WO6 nanosheets to improve the electrocatalyst for oxygen evolution reaction, *Appl. Surf. Sci.*, 2019, **478**, 969–980.

30 J. Li, X. Xu, B. Zhang, W. Hou, S. Lv and Y. Shi, Controlled synthesis and fine-tuned interface of NiS nanoparticles/Bi2WO6 nanosheets heterogeneous as electrocatalyst for oxygen evolution reaction, *Appl. Surf. Sci.*, 2020, **526**, 146718.

31 Z.-P. Nie, D.-K. Ma, G.-Y. Fang, W. Chen and S.-M. Huang, Concave Bi2WO6 nanoplates with oxygen vacancies achieving enhanced electrocatalytic oxygen evolution in near-neutral water, *J. Mater. Chem. A*, 2016, **4**, 2438–2444.

32 X. Chia and M. Pumera, Characteristics and performance of two-dimensional materials for electrocatalysis, *Nat. Catal.*, 2018, **1**, 909–921.

33 Y. Zhou, Y. Zhang, M. Lin, J. Long, Z. Zhang, H. Lin, J. C. Wu and X. Wang, Monolayered Bi2WO6 nanosheets mimicking heterojunction interface with open surfaces for photocatalysis, *Nat. Commun.*, 2015, **6**, 8340.

34 D. Yan, Y. Li, J. Huo, R. Chen, L. Dai and S. Wang, Defect Chemistry of Nonprecious-Metal Electrocatalysts for Oxygen Reactions, *Adv. Mater.*, 2017, **29**, 1606459.

35 T. Kwon, M. Jun, J. Joo and K. Lee, Nanoscale heterointerfaces between metals and metal compounds for electrocatalytic applications, *J. Mater. Chem. A*, 2019, **7**, 5090–5110.

36 M. Li, Y. Wang, Y. Zheng, G. Fu, D. Sun, Y. Li, Y. Tang and T. Ma, Gadolinium-Induced Valence Structure Engineering for Enhanced Oxygen Electrocatalysis, *Adv. Energy Mater.*, 2020, **10**, 1903833.

37 X. Long, W. Qiu, Z. Wang, Y. Wang and S. Yang, Recent advances in transition metal-based catalysts with heterointerfaces for energy conversion and storage, *Mater. Today Chem.*, 2019, **11**, 16–28.

38 J. Mao, P. Liu, C. Du, D. Liang, J. Yan and W. Song, Tailoring 2D MoS2 heterointerfaces for promising oxygen reduction reaction electrocatalysis, *J. Mater. Chem. A*, 2019, **7**, 8785–8789.

39 J. Y. Wang, W. T. Liu, X. P. Li, T. Ouyang and Z. Q. Liu, Strong hydrophilicity NiS2/Fe7S8 heterojunctions encapsulated in N-doped carbon nanotubes for enhanced oxygen evolution reaction, *Chem. Commun.*, 2020, **56**, 1489–1492.

40 Y. Wang, Y. Zou, L. Tao, Y. Wang, G. Huang, S. Du and S. Wang, Rational design of three-phase interfaces for electrocatalysis, *Nano Res.*, 2019, **12**, 2055–2066.

41 Y. Huang, R. Yang, G. Anandhababu, J. Xie, J. Lv, X. Zhao, X. Wang, M. Wu, Q. Li and Y. Wang, Cobalt/Iron(Oxides) Heterostructures for Efficient Oxygen Evolution and Benzyl Alcohol Oxidation Reactions, *ACS Energy Lett.*, 2018, **3**, 1854–1860.

42 J. X. Feng, S. H. Ye, H. Xu, Y. X. Tong and G. R. Li, Design and Synthesis of FeOOH/CeO2 Heterolayered Nanotube Electrocatalysts for the Oxygen Evolution Reaction, *Adv. Mater.*, 2016, **28**, 4698–4703.

43 S. M. Galani, A. Mondal, D. N. Srivastava and A. B. Panda, Development of RuO2/CeO2 heterostructure as an efficient OER electrocatalyst for alkaline water splitting, *Int. J. Hydrog. Energy*, 2020, **45**, 18635–18644.

44 J.-H. Kim, K. Shin, K. Kawashima, D. H. Youn, J. Lin, T. E. Hong, Y. Liu, B. R. Wygant, J. Wang, G. Henkelman and C. B. Mullins, Enhanced Activity Promoted by CeOx on a CoOx Electrocatalyst for the Oxygen Evolution Reaction, *ACS Catal.*, 2018, **8**, 4257–4265.

45 Y. Liu, C. Ma, Q. Zhang, W. Wang, P. Pan, L. Gu, D. Xu, J. Bao and Z. Dai, 2D Electron Gas and Oxygen Vacancy Induced High Oxygen Evolution Performances for Advanced Co3O4/CeO2 Nano-hybrids, *Adv. Mater.*, 2019, **31**, 1900062.

46 B. Qiu, C. Wang, N. Zhang, L. Cai, Y. Xiong and Y. Chai, CeO2-Induced Interfacial Co2+ Octahedral Sites and Oxygen Vacancies for Water Oxidation, *ACS Catal.*, 2019, **9**, 6484–6490.



47 X. Wang, S. Zhao, Y. Zhang, Z. Wang, J. Feng, S. Song and H. Zhang, CeO<sub>2</sub> nanowires self-inserted into porous Co<sub>3</sub>O<sub>4</sub> frameworks as high-performance "noble metal free" hetero-catalysts, *Chem. Sci. J.*, 2016, **7**, 1109–1114.

48 Z. Lv, H. Zhou, H. Liu, B. Liu, M. Liang and H. Guo, Controlled assemble of oxygen vacant CeO<sub>2</sub>@Bi<sub>2</sub>WO<sub>6</sub> hollow magnetic microcapsule heterostructures for visible-light photocatalytic activity, *Chem. Eng. J.*, 2017, **330**, 1297–1305.

49 Z. Zou, M. Cai, X. Zhao, J. Huang, J. Du and C. Xu, Defective metal–organic framework derivative by room-temperature exfoliation and reduction for highly efficient oxygen evolution reaction, *J. Mater. Chem. A*, 2019, **7**, 14011–14018.

50 Q. Song, J. Li, L. Wang, L. Pang and H. Liu, Controlling the Chemical Bonding of Highly Dispersed Co Atoms Anchored on an Ultrathin g-C<sub>3</sub>N<sub>4</sub>@Carbon Sphere for Enhanced Electrocatalytic Activity of the Oxygen Evolution Reaction, *Inorg. Chem.*, 2019, **58**, 10802–10811.

51 R. Wang, B. Li, Y. Xiao, X. Tao, X. Su and X. Dong, Optimizing Pd and Au-Pd decorated Bi<sub>2</sub>WO<sub>6</sub> ultrathin nanosheets for photocatalytic selective oxidation of aromatic alcohols, *J. Catal.*, 2018, **364**, 154–165.

52 M. Li, X. Pan, M. Jiang, Y. Zhang, Y. Tang and G. Fu, Interface engineering of oxygen-vacancy-rich CoP/CeO<sub>2</sub> heterostructure boosts oxygen evolution reaction, *Chem. Eng. J.*, 2020, **395**, 125160.

53 Y. Zhou, Y. Zhang, M. Lin, J. Long, Z. Zhang, H. Lin, J. C. Wu and X. Wang, Monolayered Bi<sub>2</sub>WO<sub>6</sub> nanosheets mimicking heterojunction interface with open surfaces for photocatalysis, *Nat. Commun.*, 2015, **6**, 8340.

54 S. Guan, X. Fu, Z. Lao, C. Jin and Z. Peng, NiS–MoS<sub>2</sub> heteronanosheet array electrocatalysts for efficient overall water splitting, *Sustain. Energy Fuels*, 2019, **3**, 2056–2066.

55 R. Ma, M. Jahurul Islam, D. Amaranatha Reddy and T. K. Kim, Transformation of CeO<sub>2</sub> into a mixed phase CeO<sub>2</sub>/Ce<sub>2</sub>O<sub>3</sub> nanohybrid by liquid phase pulsed laser ablation for enhanced photocatalytic activity through Z-scheme pattern, *Ceram. Int.*, 2016, **42**, 18495–18502.

56 S. Sun, W. Wang and L. Zhang, Facile preparation of three-dimensionally ordered macroporous Bi<sub>2</sub>WO<sub>6</sub> with high photocatalytic activity, *J. Mater. Chem.*, 2012, **22**, 19244.

57 H. Huang, R. Cao, S. Yu, K. Xu, W. Hao, Y. Wang, F. Dong, T. Zhang and Y. Zhang, Single-unit-cell layer established Bi<sub>2</sub>WO<sub>6</sub> 3D hierarchical architectures: Efficient adsorption, photocatalysis and dye-sensitized photoelectrochemical performance, *Appl. Catal., B*, 2017, **219**, 526–537.

58 B. Qiu, C. Wang, N. Zhang, L. Cai, Y. Xiong and Y. Chai, CeO<sub>2</sub>-Induced Interfacial Co<sup>2+</sup> Octahedral Sites and Oxygen Vacancies for Water Oxidation, *ACS Catal.*, 2019, **9**, 6484–6490.

59 G. Liu, Z. Cui, M. Han, S. Zhang, C. Zhao, C. Chen, G. Wang and H. Zhang, Ambient Electrosynthesis of Ammonia on a Core-Shell-Structured Au@CeO<sub>2</sub> Catalyst: Contribution of Oxygen Vacancies in CeO<sub>2</sub>, *Chem.*, 2019, **25**, 5904–5911.

60 R. Zhang, X. Ren, S. Hao, R. Ge, Z. Liu, A. M. Asiri, L. Chen, Q. Zhang and X. Sun, Selective phosphidation: an effective strategy toward CoP/CeO<sub>2</sub> interface engineering for superior alkaline hydrogen evolution electrocatalysis, *J. Mater. Chem. A*, 2018, **6**, 1985–1990.

61 J. Bao, X. Zhang, B. Fan, J. Zhang, M. Zhou, W. Yang, X. Hu, H. Wang, B. Pan and Y. Xie, Ultrathin Spinel-Structured Nanosheets Rich in Oxygen Deficiencies for Enhanced Electrocatalytic Water Oxidation, *Angew. Chem., Int. Ed.*, 2015, **54**, 7399–7404.

62 C. Guo, Y. Zheng, J. Ran, F. Xie, M. Jaroniec and S. Z. Qiao, Engineering High-Energy Interfacial Structures for High-Performance Oxygen-Involving Electrocatalysis, *Angew. Chem., Int. Ed.*, 2017, **56**, 8539–8543.

63 Y. Jiao, Y. Zheng, M. Jaroniec and S. Z. Qiao, Design of electrocatalysts for oxygen- and hydrogen-involving energy conversion reactions, *Chem. Soc. Rev.*, 2015, **44**, 2060–2086.

64 B. Liu, H. Q. Peng, C. N. Ho, H. Xue, S. Wu, T. W. Ng, C. S. Lee and W. Zhang, Mesoporous Nanosheet Networked Hybrids of Cobalt Oxide and Cobalt Phosphate for Efficient Electrochemical and Photoelectrochemical Oxygen Evolution, *Small*, 2017, **13**, 1701875.

65 C. C. McCrory, S. Jung, I. M. Ferrer, S. M. Chatman, J. C. Peters and T. F. Jaramillo, Benchmarking hydrogen evolving reaction and oxygen evolving reaction electrocatalysts for solar water splitting devices, *J. Am. Chem. Soc.*, 2015, **137**, 4347–4357.

66 F. Lyu, Y. Bai, Z. Li, W. Xu, Q. Wang, J. Mao, L. Wang, X. Zhang and Y. Yin, Self-Templated Fabrication of CoO–MoO<sub>2</sub> Nanocages for Enhanced Oxygen Evolution, *Adv. Funct. Mater.*, 2017, **27**, 1702324.

67 X. Shang, K. L. Yan, Y. Rao, B. Dong, J. Q. Chi, Y. R. Liu, X. Li, Y. M. Chai and C. G. Liu, In situ cathodic activation of V-incorporated Ni<sub>x</sub>Si<sub>y</sub> nanowires for enhanced hydrogen evolution, *Nanoscale*, 2017, **9**, 12353–12363.

68 M. Lee, H.-S. Oh, M. K. Cho, J.-P. Ahn, Y. J. Hwang and B. K. Min, Activation of a Ni electrocatalyst through spontaneous transformation of nickel sulfide to nickel hydroxide in an oxygen evolution reaction, *Appl. Catal., B*, 2018, **233**, 130–135.

69 L. L. Feng, G. Yu, Y. Wu, G. D. Li, H. Li, Y. Sun, T. Asefa, W. Chen and X. Zou, High-index faceted Ni<sub>3</sub>S<sub>2</sub> nanosheet arrays as highly active and ultrastable electrocatalysts for water splitting, *J. Am. Chem. Soc.*, 2015, **137**, 14023–14026.

